Asian Journal of Chemistry; Vol. 38, No. 4 (2026), 1095-1104
ASIAN JOURNAL OF CHEMISTRY
https://doi.org/10.14233/ajchem.2026.35451

Structural, Optical, Photocatalytic and Antibacterial Properties of Hydrothermally Synthesised CuO–WO_3 Heterojunction Nanocomposite

RAJENDRA PRASAD JAKKULA[1,2], DOMALA SURESH[1,*], SRINIVASA RAO KONDA[3] and RAMYASHREE RAGHAVAPURAM[1]

[1]Department of Physics and Electronics, Chaitanya (Deemed to be University), Hyderabad-500075, India
[2]Science Lab, Department of Physics, Government Polytechnic, Warangal-506007, India
[3]Department of Physics, Indian Institute of Technology Ropar, Rupnagar-140001, India

*Corresponding author: E-mail: suresh.domala@chaitanya.edu.in

Received: 13 December 2025 *Accepted*: 27 March 2026 *Published online*: 8 April 2026 AJC-22333

Nanostructured pure CuO and CuO-WO_3 heterojunction composites were synthesised using a hydrothermal technique. The materials were analysed by XRD, SEM, TEM, AFM, EDX and FTIR to determine their physico-chemical properties. Monoclinic crystal structure and heterojunction composite that developed between the synthesised CuO and WO_3 are indicated. The photocatalytic activity was investigated *via* the degradation of methylene blue under visible light, where the CuO–WO_3 nanocomposite exhibited higher photocatalytic activity compared to the unmodified nanostructured CuO. The enhanced photocatalytic activity of the composite material is attributed to the suppressed recombination of photogenerated electron–hole pairs under visible-light irradiation and the increased generation of reactive oxygen species (ROS) facilitated by the presence of WO_3. The antibacterial performance of the prepared materials was evaluated against Gram-positive and Gram-negative bacteria. In comparison to unmodified CuO, the CuO–WO_3 nanocomposite demonstrated superior antibacterial activity due to better surface deposition and ROS-mediated bacterial cell membrane destruction, which was attributed to the interaction of the generated ROS with the cell membranes of bacteria. The enhanced performance is attributed to improved interfacial charge transfer, heterojunction-induced carrier separation and increased surface-active sites. The CuO–WO_3 system demonstrates the significance of interfacial engineering and phase coupling in tailoring functional properties. These findings highlight the potential of such oxide-based composites as multifunctional agents for advanced environmental and antimicrobial applications.

Keywords: Heterojunction nanocomposites, Photocatalysis, Antibacterial activity, Wastewater treatment, Visible light activity.

INTRODUCTION

The environment is polluted due to rapid population growth and industrialisation, particularly from releasing toxic chemicals or organic dyes through freshwater channels. The synthetic dyes, which include methylene blue (MB), have many uses in the printing industry, textile industry and medicine; since they are chemically stable and resistant to biodegradation, they are difficult to remove from the environment by traditional treatments [1]. Photocatalysis using metal oxides and their composites has emerged as a viable, inexpensive and environmentally-safe way to degrade organic pollutants [2-6]. Due to the rapid spread of pathogenic bacteria and associated global health issues, there is a requirement for effective antibacterial materials for environmental remediation and medical applications.

Metal oxides and their composites are an important class of materials for environmental and biological applications due to their optical, structural and electrical properties. The interaction between metal and oxygen ions, which is influenced by the oxidation state of different metals, coordination geometry and crystal structure, gives rise to their various functionalities. Metal oxides have a variety of structures, including rutile, wurtzite, spinel and perovskite, which have a significant impact on their chemical and physical properties [2,7-9]. In view of their exceptional physico-chemical characteristics and multifunctional capabilities, metal oxide nanoparticles have advanced environmental science and technology. Metal oxide nanoparticles' superior properties, such as their small particle size, high surface reactivity, chemical stability and thermal stability, give them their versatility. Because of these characteristics, they can effectively interact with pollutants and take

part in catalytic reactions, which makes them ideal for environmental remediation procedures [10,11].

Among the metal oxides that have received substantial attention is CuO, which is a p-type semiconductor that has excellent properties for photocatalytic applications, for example, absorption of visible-light, tunable bandgap and strong redox activity. Brisk recombination of charge carriers is a serious problem for nearly all photocatalysts; however, it is particularly problematic for CuO nanoparticle photocatalysts, as shown by both theoretical and experimental studies [3,4, 12-15]. Heterojunction composite engineering has been extensively utilised as an effective method for alleviating the limitations of photocatalysis in the attempt to enhance the photocatalytic efficiency of a catalyst through a composite heterostructure of two semiconductors with proper band alignment. This makes it possible to create heterostructure composite photocatalysts, which significantly improve charge carrier separation efficiency, increase charge carrier longevity and promote higher production of reactive oxygen species upon exposure to visible light [16,17]. An n-type semiconductor possessing a narrow band gap (2.4-2.9 eV) and high chemical stability and strong resistance to photo corrosion is tungsten trioxide (WO_3) is an excellent candidate for use in the visible-light-driven photocatalytic and environmental remediation applications [5,18]. However, the photocatalytic efficiency of pure WO_3 is subpar due of its low conduction band location and the quick recombination of charge carriers generated photogenically [19-21].

Single-component oxides such as CuO and WO_3, despite significant advancements in semiconductor catalysts, face barriers to improved efficiency attributed to issues like rapid recombination of electron–hole pairs, non-optimal band edge alignment and poor utilisation of visible light. The formation of composite p–n heterojunctions constructed with semiconductors has the potential to facilitate interfacial charge separation, ultimately leading to improved photocatalytic and antibacterial activity. Thus, the nanostructured composites composed of CuO and WO_3 exhibit significant photocatalytic and antibacterial activity through multiple mechanisms, *viz*. photocatalytic remediation of contaminated environments and ability to kill both Gram-positive and Gram-negative bacteria. ROS-induced intracellular oxidative stress is the main factor affecting these antibacterial actions like membrane rupture and hence, intracellular damage [22-24]. The heterojunction metal oxide composites possess multiple properties, with ROS being an important component for photocatalytically degrading dye molecules as well as exhibiting antimicrobial activity.

In view of above facts, the authors aimed to synthesize pure CuO and CuO-WO_3 nanocomposites *via* hydrothermal method and characterised for their physico-chemical properties. The photocatalytic performance of the prepared samples was examined in degrading the methylene blue dye under visible light irradiation. Also, the antibacterial activity of the prepared samples against both Gram-positive (*Bacillus*) and Gram-negative (*E. coli*) microorganisms was evaluated.

EXPERIMENTAL

All reagents and chemicals employed in the synthesis were of analytical quality and used as such. Sodium tungstate dihydrate, sodium hydroxide, ethanol and copper(II) 2,4-pentanedionate were purchased from the reputed commercial chemical suppliers. Double-distilled water was used to prepare all the solutions.

Synthesis of pure CuO: Using a hydrothermal method, the CuO nanostructures were synthesized using copper(II) acetylacetonate as precursor of copper. In a typical procedure, 3 g of Cu(II) acetylacetonate was dissolved in solvent and 0.3 g of NaOH was added gradually while shaking constantly. The uniform mixture was heated to 180 ºC for 8 h in a stainless-steel autoclave, which was allowed to cool naturally to room temperature after 8 h. The black precipitate was filtered and repeatedly washed with distilled water and ethanol to remove residual organic and inorganic impurities. Final product was left to dry naturally at 60 ºC for 20 h before using the product.

Synthesis of CuO–WO_3 nanocomposite: The CuO-WO_3 composite was produced by dissolving 3 g of copper(II) acetylacetonate ($Cu(C_5H_7O_2)_2$) and 1 g of sodium tungstate dihydrate ($Na_2WO_4{\cdot}2H_2O$) in a reaction mixture. Then, 0.3 g NaOH was added with constant stirring to obtain a clear homogeneous solution. The solution was then heated to 180 ºC for 8 h in a stainless-steel autoclave. It was now time to let the autoclave cool to ambient temperature. The final material was dried at 60 ºC for 20 h to remove moisture under normal conditions after the precipitate was collected and repeatedly washed (until all impurities were eliminated) with distilled water and 100% ethanol. The hydrothermal method was selected due to its effectiveness in producing uniform composite nanostructures with controlled morphology and strong interfacial bonding between constituent phases.

Characterisation: The structural characteristics of the synthesized materials were examined using powder X-ray diffraction (XRD) recorded on a Bruker D8 Advance diffractometer with Cu*K*α radiation (λ = 1.5406 Å) in the 2θ range of 20º-70º. The surface morphology and microstructural characteristics were investigated using scanning electron microscopy (SEM) on a JEOL JSM-7610F field-emission scanning electron microscope, while the elemental composition and distribution of the constituent elements were determined using an energy-dispersive X-ray analysis (EDAX) system coupled with the SEM instrument. The optical absorption behaviour and electronic transitions of the prepared samples were analysed using UV-Visible spectroscopy on a Shimadzu UV-2600 UV-Vis spectrophotometer. The identification of functional groups within the synthesized materials were carried out using Fourier transform infrared (FTIR) spectroscopy recorded on a Bruker Alpha FTIR spectrometer in the spectral range of 4000-400 cm^{-1}. In addition, the particle size, morphology, and shape at higher resolution were studied using transmission electron microscopy (TEM) performed on a JEOL JEM-2100 micro-scope operated at 200 kV.

Photocatalysis: To examine the photocatalytic degradation efficiency of the prepared samples in degrading MB dye, a simulated solar irradiation using a 300 W xenon arc lamp provided with an ultraviolet cutoff filter (λ > 420 nm) was employed to establish visible light driven reactions. The light intensity was calibrated to 100 mW/cm^2 with a fixed distance maintained between the light source and the reactor vessel. To achieve equilibrium, 100 mL of 10 ppm of dye

solution containing 50 mg of catalyst were stirred for 30 min. The photocatalytic degradation tests were conducted for every 0.5 h. At regular time intervals, 5 mL of reaction mixture was pipetted into Amber-coloured vials and then the concentration was measured using a UV-vis spectrophotometer. The following equation was used to obtain the percentage of degradation [25]:

$$D\ (\%) = \frac{C_o - C}{C_o} \times 100 \quad (1)$$

where C_o and C designate the initial concentration of MB dye at a time 't' = '0' and concentration of MB dye at a time 't' = 't', respectively.

Antibacterial activity: The experiment was conducted using a disc diffusion assay on Muller-Hinton agar media. A swab was used to evenly spread one milliliter of an actively growing bacterial inoculums having an estimated microbial load of 10^7 CFU mL^{-1} (0.5 McFarland Standard) on the agar medium. In order to absorb any surface moisture, before the samples were applied, inoculated plates were kept at room temperature for 6 min. The samples containing 50 mg mL^{-1} were prepared in 10% DMSO at the same time and put onto autoclaved filter paper discs of 6 mm diameter, followed by placement of the nanostructures on inoculated Mueller-Hinton agar plates after being absorbed by the filter paper. The negative control was a paper disc soaked in 10% DMSO and the positive control was 15 μg of erythromycin. Post incubation (24 h, 37 ºC), the inhibition diameters were determined in mm.

RESULTS AND DISCUSSION

XRD studies: Fig. 1a-b shows the XRD patterns of pure CuO and CuO–WO_3 nanocomposite, both exhibiting similar main diffraction peaks and virtually equal corresponding 2θ positions. Fig. 1a shows the XRD pattern of pure CuO, with diffraction peaks at 2θ ≈ 35.4º, 38.7º, 48.8º and 61.4º corresponding to the (002), (111), $(20\bar{2})$ and $(11\bar{3})$ planes of monoclinic CuO (JCPDs card no. 48-1548) [23,24]. It confirms that the synthesised CuO sample possess a monoclinic structure and consist of a single-phase CuO.

Fig. 1b shows the XRD pattern of the synthesised CuO–WO_3 nanocomposite, which correspond to a monoclinic phase and can be indexed to monoclinic WO_3 (JCPDS No. 01-072-1465), confirming the crystalline nature of the material. The predominant peaks positions (111) indicate $WO_{2.95}$ and (111), (031), (110), (222) and (113) in the diffraction pattern clearly define the monoclinic phase of WO_3 [26]. After adding WO_3, the peak intensity and broadening change slightly, this implies a strong interaction between CuO and WO_3 forms a heterojunction composite [27]. The observed peak modifications and slight broadening confirm the successful formation of a coupled composite system, where interfacial interactions between CuO and WO_3 phases contribute to structural stability and enhanced functional behaviour.

EDS studies: The elemental composition of pure CuO and CuO–WO_3 composite was examined using energy-dispersive X-ray spectroscopy (EDS). The quantitative results, expressed in terms of weight percentage and atomic percentage, provide insight into the relative proportions and distribution of elements such as oxygen (O), copper (Cu) and tungsten (W). The EDS spectrum of CuO (Fig. 2a) shows two peaks corresponding to oxygen (O K) and copper (Cu L). The weight percentages are 33.56% for O and 66.44% for Cu, whereas the atomic percentages are 68.40% and 31.60%, respectively. The higher atomic percentage of oxygen indicates that the sample surface is rich in oxygen, suggesting the possible formation of a copper oxide phase. Since copper has a higher atomic mass, its weight percentage appears larger despite its lower atomic count compared to oxygen. In case of CuO–WO_3 (Fig. 2b), the composition includes O, Cu and a small fraction of tungsten (W). The weight percentages were 24.61% O, 71.02% Cu and 4.37% W, while the atomic percentages were 57.09%, 41.46% and 1.44%, respectively. The presence of tungsten, although minor, may be attributed to the incorporation of tungsten species from the precursor during the hydrothermal synthesis. The reduced oxygen content compared to pure CuO suggests a lower oxidation level of copper or a more metallic nature of the surface. The relatively high Cu content indicates that this sample might be more conductive or less oxidised. Neither sample showed any signs of impurities, which means that the produced nanostructures are quite pure.

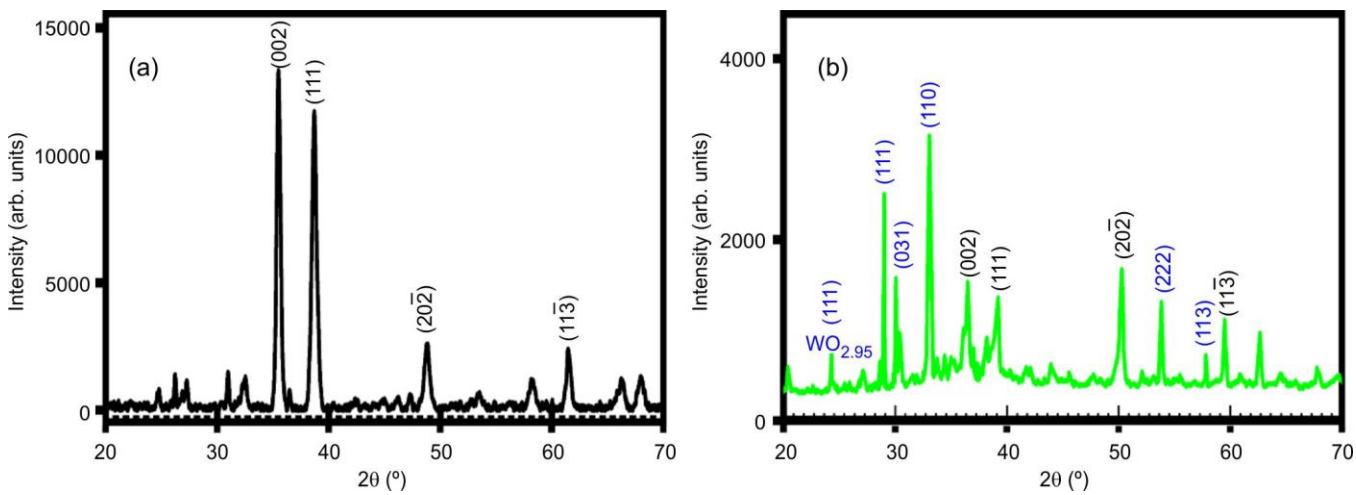

Fig. 1. XRD patterns of (a) pure CuO and (b) CuO–WO_3 nanocomposite

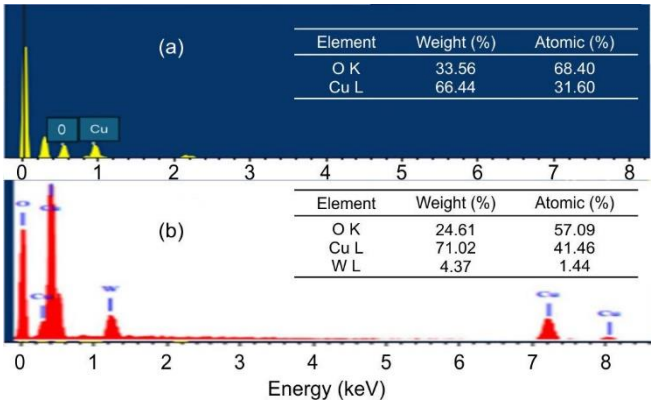

Fig. 2. EDS images of (a) pure CuO and (b) CuO-WO_3 nanocomposite

The variations across samples indicate the progressive compositional modifications likely due to changes in synthesis or post-treatment conditions, affecting oxidation state and dopant incorporation. In the CuO-WO_3 nanocomposite system, the charge separation and reduction of the recombination of charge carriers will be promoted by the presence of tungsten by heterojunction formation.

SEM studies: The surface characteristics of the pure CuO and CuO–WO_3 nanocomposite were formed and studied using SEM technique. Nanoparticles are closely packed together to create clusters with irregular morphologies, as observed in the SEM image of pure CuO (Fig. 3a). Such aggregation is commonly observed in hydrothermally synthesized metal oxide nanostructures due to their high surface energy, which promotes strong interparticle interactions. While agglomeration can facilitate the formation of interconnected networks that enhance charge transfer during photocatalytic processes, it may also hinder uniform particle dispersion.

However, the surface of the CuO–WO_3 nanocomposite is rougher and more porous and the assemblies of linked nanoparticles are dispersed over a larger area. The effective surface area and number of active sites are significantly increased by this porous structure, this facilitates the dye molecules' attachment to the surface and eventual breakdown when exposed to visible light [19,20].

TEM studies: Fig. 4a-b showed an internal morphology, nanoscale structure about CuO and CuO-WO_3 nanocomposites, revealing aggregated nanoparticles with irregular shapes and sizes below 100 nm, confirming their nanocrystalline nature. In the CuO-WO_3 nanocomposite, distinct contrast differences indicate the coexistence of CuO and WO_3 phases with close interfacial contact, suggesting the formation of a heterojunction structure. This intimate interface promotes efficient charge separation and reduces electron–hole recombination, while the aggregated yet uniformly distributed nanocrystallites provide increased active surface sites and facilitate interfacial charge transfer. The incorporation of WO_3 into the CuO matrix therefore leads to a heterostructured composite with enhanced surface roughness and improved photocatalytic potential.

FTIR studies: FTIR spectra of pure CuO and CuO-WO_3 nanocomposites are displayed in Fig. 5a-b. FTIR spectrum of pure CuO shows a strong band at ~3442 cm^{-1} due to O–H stretching of surface hydroxyls or H_2O, which helps generate $^{\bullet}OH$ radicals in the antibacterial process and photocatalytic dye degradation [2,4,28]. The weak absorption bands in CuO around 2915 and 2335 cm^{-1} attributed to C–H vibrations and atmospheric CO_2, respectively, while the band near 1614 cm^{-1} corresponds to H–O–H bending of adsorbed water molecules. The peaks observed at approximately 1386 and 1043 cm^{-1} are assigned to OH bending and C–OH stretching vibrations, indicating the presence of surface hydroxyl groups. These hydroxyl functionalities enhance adsorption of reactant species and contribute to improved photocatalytic and antibacterial activity [15,29]. The strong absorption bands in the region 621-525 cm^{-1} are associated with Cu–O stretching vibrations, confirming the formation of monoclinic CuO nanostructures.

The FTIR spectrum of the CuO–WO_3 nanocomposite retains most characteristic bands of CuO, indicating preservation of the host structure after WO_3 incorporation. The broad O–H stretching band around 3433 cm^{-1} and the H–O–H bending vibration near 1614 cm^{-1} confirm the presence of surface hydroxyl groups. Bands at ~1386 cm^{-1} and 1043-1008 cm^{-1} correspond to C–OH stretching and OH bending vibrations. A new absorption band appearing in the range 921-824 cm^{-1} is assigned to W–O–W stretching vibrations, confirming

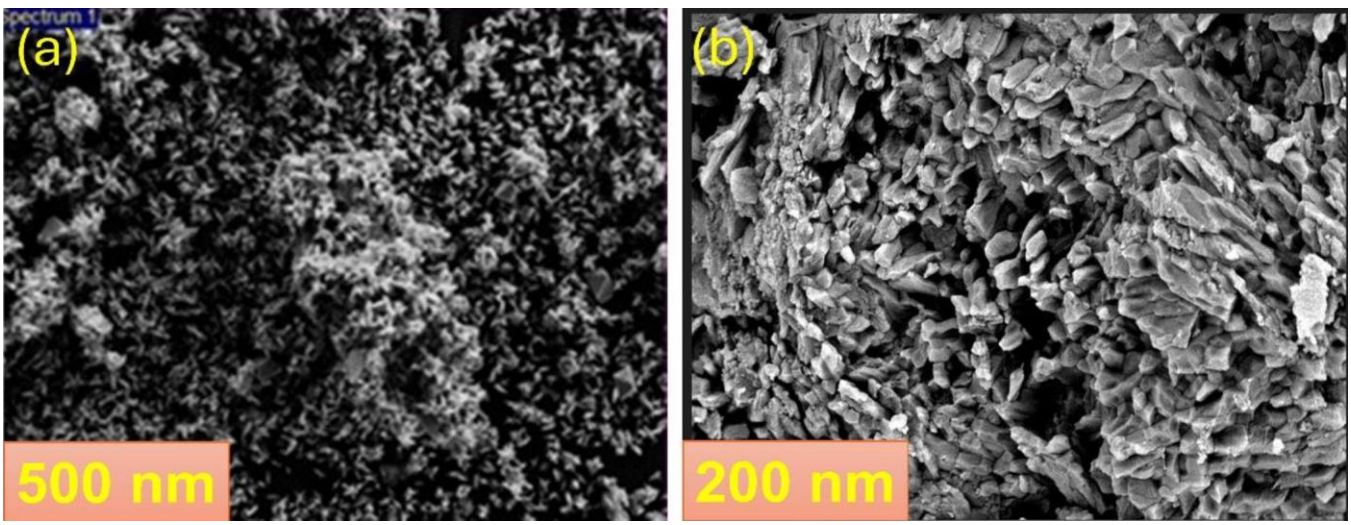

Fig. 3. SEM images of (a) pure CuO and (b) CuO-WO_3 nanocomposite

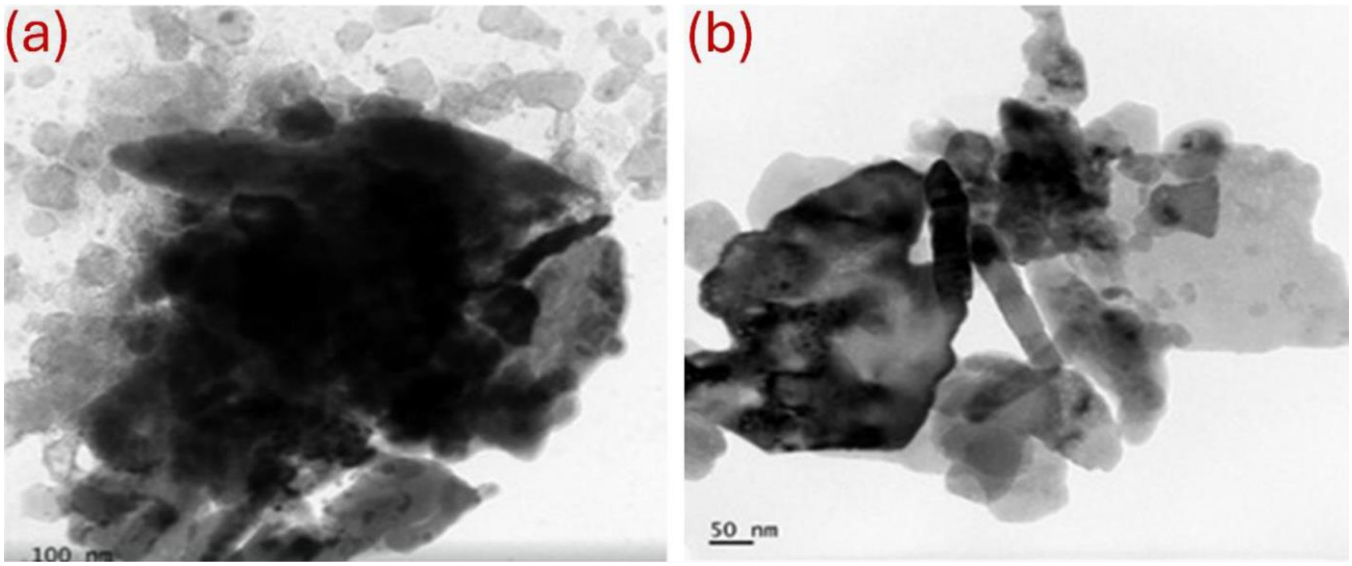

Fig. 4. TEM images of (a) pure CuO and (b) CuO–WO_3 nanocomposite

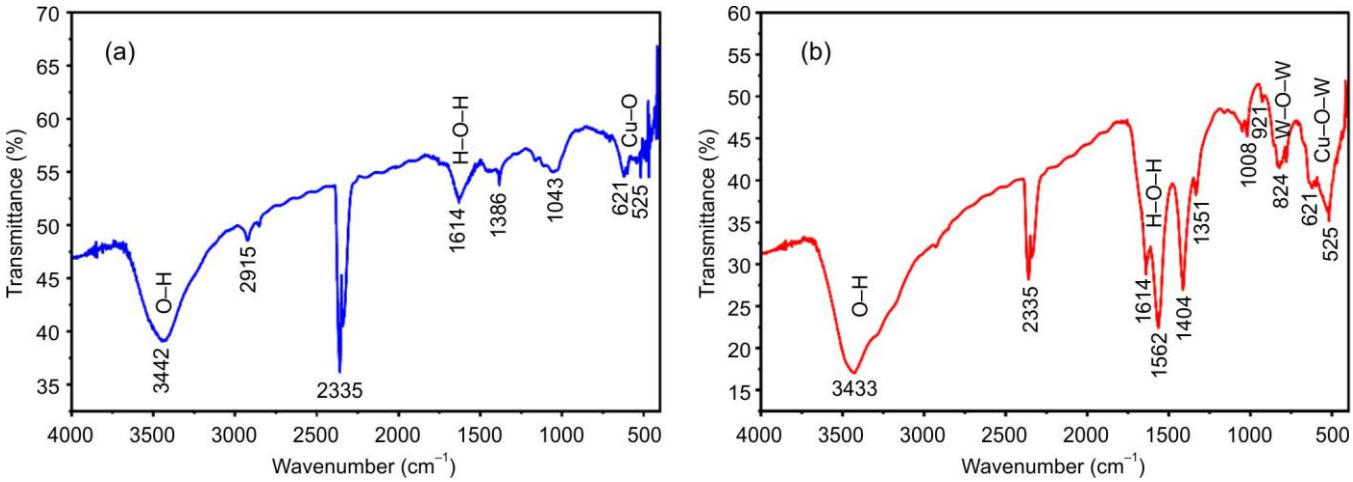

Fig. 5. FTIR spectra of (a) pure CuO and (b) CuO-WO_3 nanocomposite

successful incorporation of WO_3 into the CuO matrix [20]. Furthermore, the broad band in the 700-500 cm^{-1} region arises from overlapping Cu–O and W–O vibrations [30]. The shift of the Cu–O band from ~530 cm^{-1} in pure CuO to ~560 cm^{-1} in the nanocomposite indicates strong interfacial interaction and heterojunction formation between CuO and WO_3.

AFM studies: Fig. 6a shows the AFM image of pure CuO, revealing a relatively homogeneous surface with uniformly distributed nanoscale protrusions and grains across the matrix. The measured surface roughness lies between 12 and 15 nm, indicating systematic grain growth and dense packing of particles. Such a uniform morphology supports stable charge transport and reduces trapping of charge carriers at surface defects, which is beneficial for photocatalytic applications [16,17]. Moreover, the moderate surface roughness provides sufficient surface area for adsorption of dye molecules, developing the additional active sites for catalytic reactions and facilitating the generation of reactive oxygen species (ROS) through surface hydroxyl groups. However, compared to nanocomposite systems, the relatively lower roughness may limit the number of active sites and overall catalytic efficiency [4].

Fig. 6b presents the AFM image of the CuO-WO_3 nanocomposite, which exhibits a more heterogeneous surface with sharper protrusions, uneven grain distribution, and larger peak-to-valley variations. The surface roughness increases to approximately 25-30 nm, indicating nanoparticle aggregation and effective coupling between CuO and WO_3 phases, consistent with heterojunction formation [19]. The increased roughness enhances surface area, improves adsorption of reactant species and facilitates interfacial charge transfer. The rough and irregular surface morphology enhances interaction with the bacterial membranes, while increased ROS generation induces oxidative stress, thereby improving antibacterial activity of the CuO–WO_3 composite compared to pure CuO [12].

UV-Visible spectral studies: Fig. 7 shows the absorption behaviour of the prepared materials. The pure CuO sample exhibits an absorption edge around 410 nm, extending approximately from 400 to 550 nm. In the CuO–WO_3 nanocomposite, a noticeable red shift in the absorption edge is observed compared to pure CuO, indicating enhanced absorption in the visible region. This shift suggests that incorporation of WO_3 reduces the band gap energy and improves light harvesting ability of

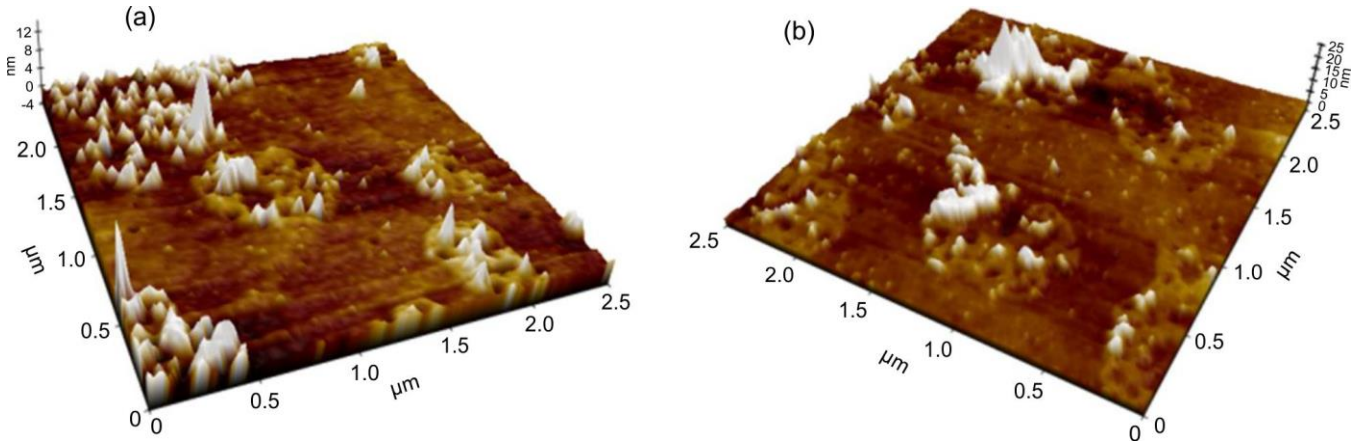

Fig. 6. AFM images of (a) pure CuO and (b) CuO-WO_3 nanocomposite

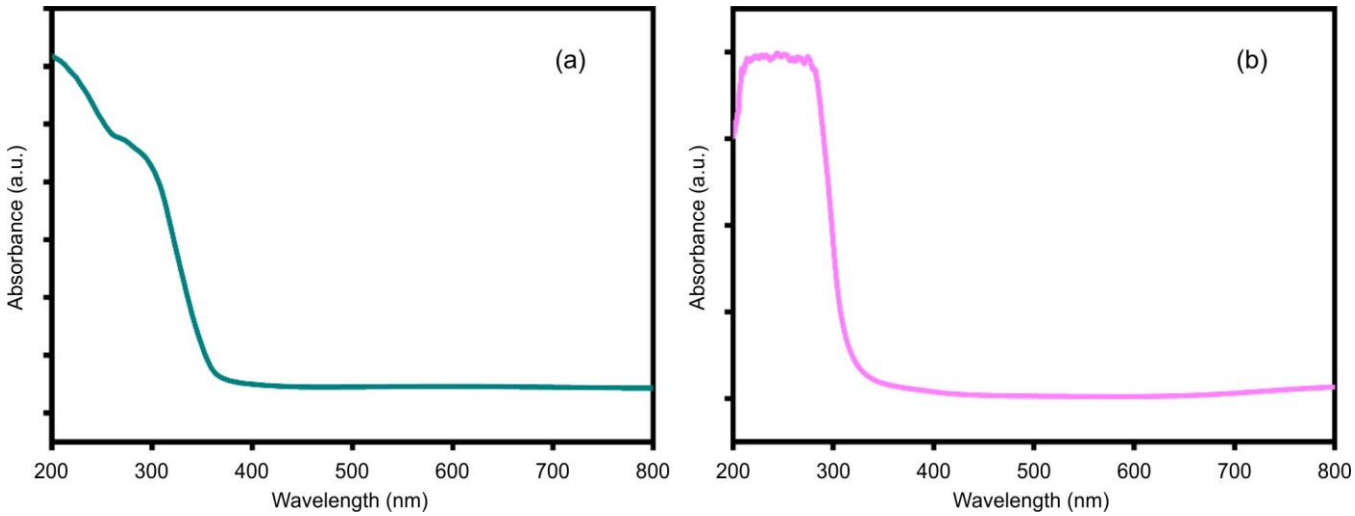

Fig. 7. Absorption spectra of (a) pure CuO and (b) CuO–WO_3 nanocomposite

the nanocomposite. Similar red shift behaviour with dopant incorporation has also been reported in earlier studies [31].

The optical band gap values were determined using the Tauc relation by extrapolating the linear portion of the $(\alpha h\nu)^2$ *versus* $h\nu$ plots to $\alpha = 0$, as shown in Fig. 8 [25]. The estimated band gap values for pure CuO and CuO–WO_3 nanocomposite were found to be 3.02 eV and 2.97 eV, respectively. These values lie within the typical range of 2.5-3.0 eV reported for similar oxide-based nanostructures [19,32]. The slight decrease in band gap for the CuO–WO_3 composite confirms

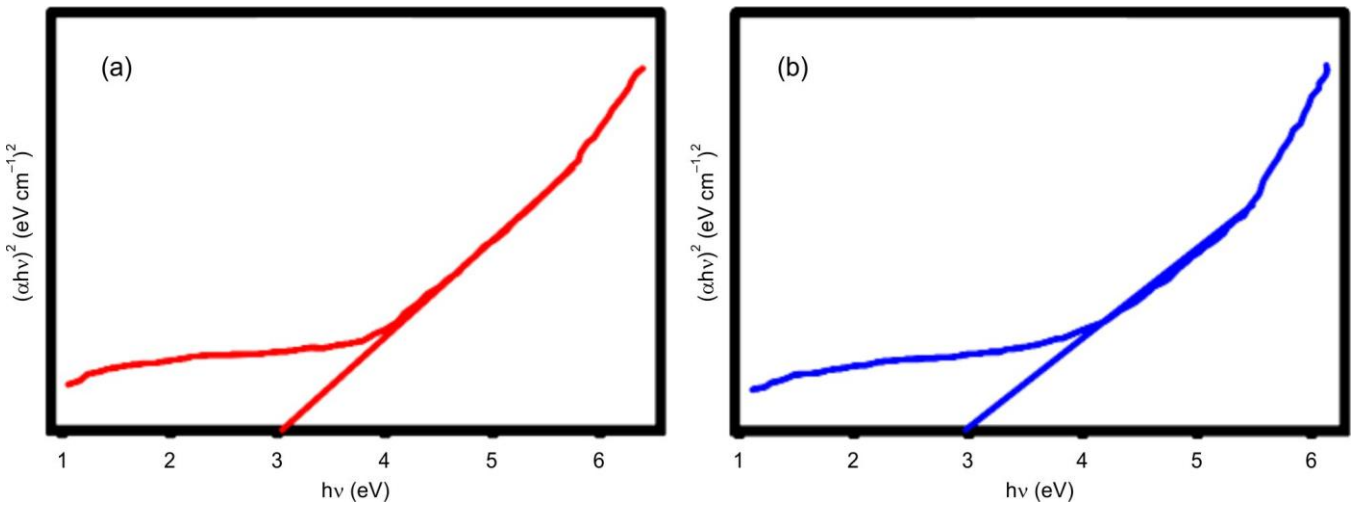

Fig. 8. Tauc plot of (a) pure CuO and (b) CuO-WO_3 nanocomposite

that incorporation of WO_3 modifies the electronic structure and enhances visible light absorption. Such band gap narrowing is advantageous for the photocatalytic and environmental remediation applications, as it promotes improved utilization of visible light and facilitates charge transfer processes.

Photocatalytic degradation studies: The photocatalytic degradation of methylene blue (MB) dye was evaluated using UV–Visible absorption spectroscopy. Blank experiments were carried out under identical irradiation conditions in the absence of CuO and CuO–WO_3 catalysts to verify that any change in dye concentration was due to photocatalysis rather than photolysis. Only negligible degradation was observed without catalysts, confirming that self-decomposition of MB under light irradiation is minimal.

The characteristic absorption peak of MB at ~ 660 nm gradually decreases with irradiation time, indicating progressive dye degradation. In case of pure CuO (Fig. 9a), only limited reduction in absorption intensity is observed after 180 min, suggesting comparatively lower photocatalytic efficiency. In contrast, the CuO–WO_3 nanocomposite (Fig. 9b) exhibits a much sharper decline in absorption intensity, demonstrating enhanced photocatalytic activity. The improved performance of the composite can be attributed to the increased number of active surface sites and efficient charge separation at the CuO–WO_3 heterojunction, which promotes degradation of dye molecules.

The degradation efficiency is also influenced by catalyst concentration, as adequate active sites facilitate adsorption and decomposition of pollutants, whereas excessive loading may reduce effectiveness due to aggregation and light shielding. The increased degradation efficiency observed for the CuO–WO_3 nanocomposite indicates the presence of abundant active sites and improved surface interaction with MB dye. To further evaluate the degradation behaviour and compare photocatalytic performance, the reaction kinetics were analysed using a pseudo-first-order kinetic model [33]:

$$\ln\left(\frac{C_o}{C}\right) = kt \qquad (2)$$

where k is the rate constant, C_o is the initial dye concentration and C is the concentration at irradiation time t.

The variation of C/C_o with irradiation time (Fig. 10a) indicates that the CuO–WO_3 photocatalyst exhibits a much faster decrease in dye concentration compared to pure CuO,

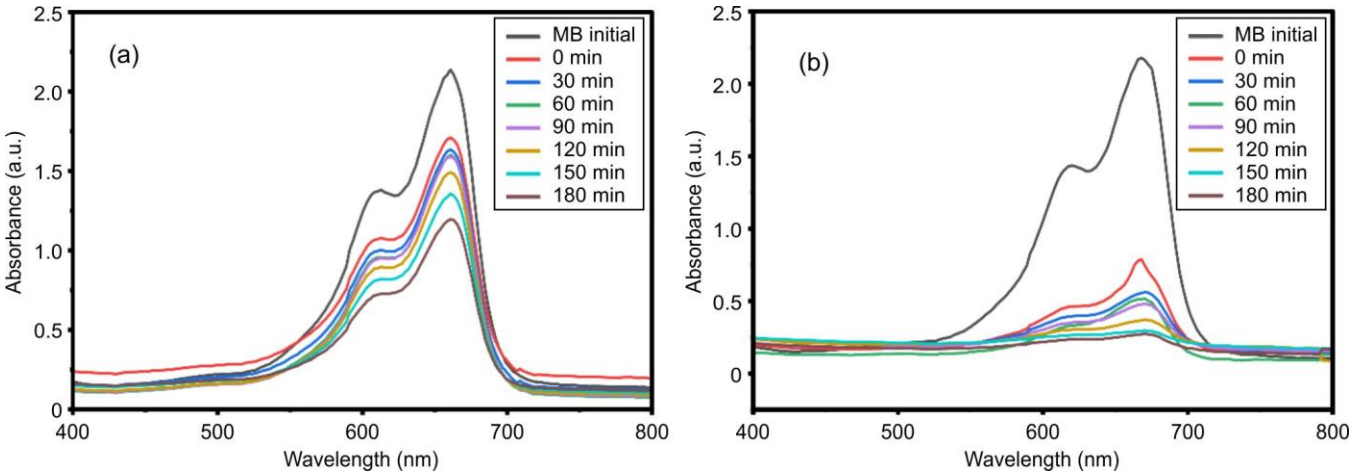

Fig. 9. UV-visible absorption spectra showing the photodegradation of MB dye, by using (a) pure CuO, (b) CuO–WO_3 nanocomposite

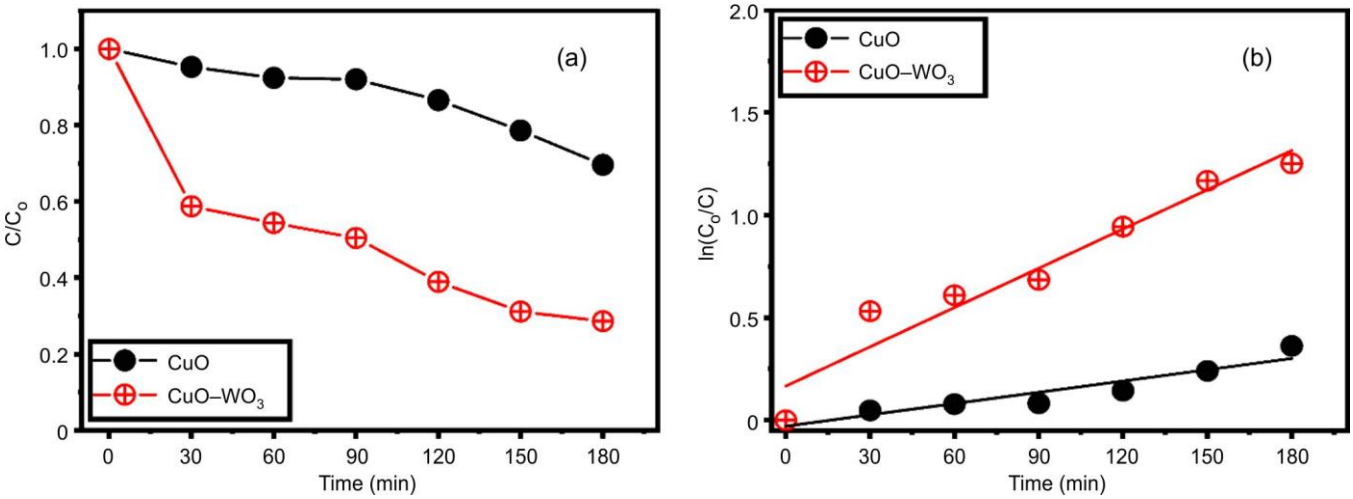

Fig. 10. Using pure CuO and CuO–WO_3 nanocomposite (a) photocatalytic degradation profile of MB dye and (b) pseudo-first-order kinetics plot

indicating superior photocatalytic activity (Fig. 10a). The linear analysis confirms that the photocatalytic degradation behaviour follows pseudo-first-order kinetics. Dependence of $\ln(C_0/C)$ on irradiation time, where the rate constants of 0.00183 min^{-1} for CuO and 0.00638 min^{-1} for CuO–WO_3 are obtained from the slopes of the fitted lines (Fig. 10b). The higher rate constant for CuO-WO_3 suggests increased photocatalytic activity and faster degradation of methylene blue dye. The higher linear regression coefficient (R^2 = 0.93533) for CuO-WO_3 compared to CuO (R^2 = 0.89272) confirms a better fit to the kinetic model.

Photocatalytic degradation mechanism: The photocatalytic process is governed by excitation of semiconductor electrons when irradiated with photons having energy equal to or greater than the band gap (ΔE). Upon illumination, the electrons are promoted from the valence band (VB) to the conduction band (CB), leaving behind holes (h^+) in the valence band. These photogenerated charge carriers participate in redox reactions with adsorbed oxygen and organic pollutants, leading to oxidative degradation of contaminants [3].

In pure CuO, the relatively wider band gap and the synthesis induced surface defects, such as oxygen vacancies, promote rapid electron–hole recombination, which limits the photocatalytic efficiency [15,34]. In contrast, incorporation of WO_3 into the CuO matrix forms a CuO–WO_3 heterojunction, resulting in modification of the band structure and improved optical response. The heterojunction generates an internal electric field at the interface, which facilitates the effective separation of photogenerated charge carriers and suppresses recombination.

This interfacial interaction is supported by structural characterizations (SEM, TEM and FTIR), which confirm the successful coupling between CuO and WO_3 phases. The improved charge separation and enhanced visible light absorption in the nanocomposite therefore lead to superior photocatalytic performance compared to pure CuO.

$$\text{Catalyst} + h\nu \rightarrow e^- + h^+$$

$$h^+ + H_2O \rightarrow {}^\bullet OH$$

$$e^- + O_2 \rightarrow {}^\bullet O_2^-$$

$$MB_{(adsorbed)} + {}^\bullet OH/{}^\bullet O_2^- \rightarrow \text{Intermediates} \rightarrow H_2O + CO_2$$

The photocatalytic mechanism of pure CuO and CuO–WO_3 nanocomposite involves light absorption, charge carrier separation and generation of reactive oxygen species under visible light irradiation. CuO is a p-type semiconductor with a band gap of approximately 3.02 eV, enabling absorption in the visible region. Upon illumination, electrons are excited from the valence band (VB) to the conduction band (CB), leaving holes (h^+) in the VB. These photogenerated carriers participate in redox reactions, where holes oxidize surface-adsorbed water to produce hydroxyl radicals ($^\bullet OH$), while electrons reduce dissolved oxygen to generate superoxide radicals ($^\bullet O_2^-$). These reactive species subsequently degrade dye molecules into harmless products such as CO_2 and H_2O [35]. However, in pure CuO, rapid recombination of electron–hole pairs limits photocatalytic efficiency [36,37].

In the CuO–WO_3 nanocomposite, coupling of p-type CuO with n-type WO_3 forms a heterojunction that promotes the spatial separation of charge carriers. Under visible light irradiation, both semiconductors absorb photons and electrons transfer from the conduction band of CuO to that of WO_3, while holes migrate from the valence band of WO_3 to the valence band of CuO. This charge redistribution suppresses recombination and prolongs carrier lifetime, resulting in enhanced generation of $^\bullet OH$ and $^\bullet O_2^-$ radicals. Consequently, the heterojunction structure significantly improves the photocatalytic degradation efficiency compared to pure CuO (Fig. 11).

Antibacterial assay: Compared to pure CuO, the CuO–WO_3 nanocomposite exhibits a significantly larger zone of inhibition, indicating enhanced antibacterial activity (Table-1). This improvement is attributed to the formation of a CuO–WO_3 heterojunction, which promotes the generation of reactive

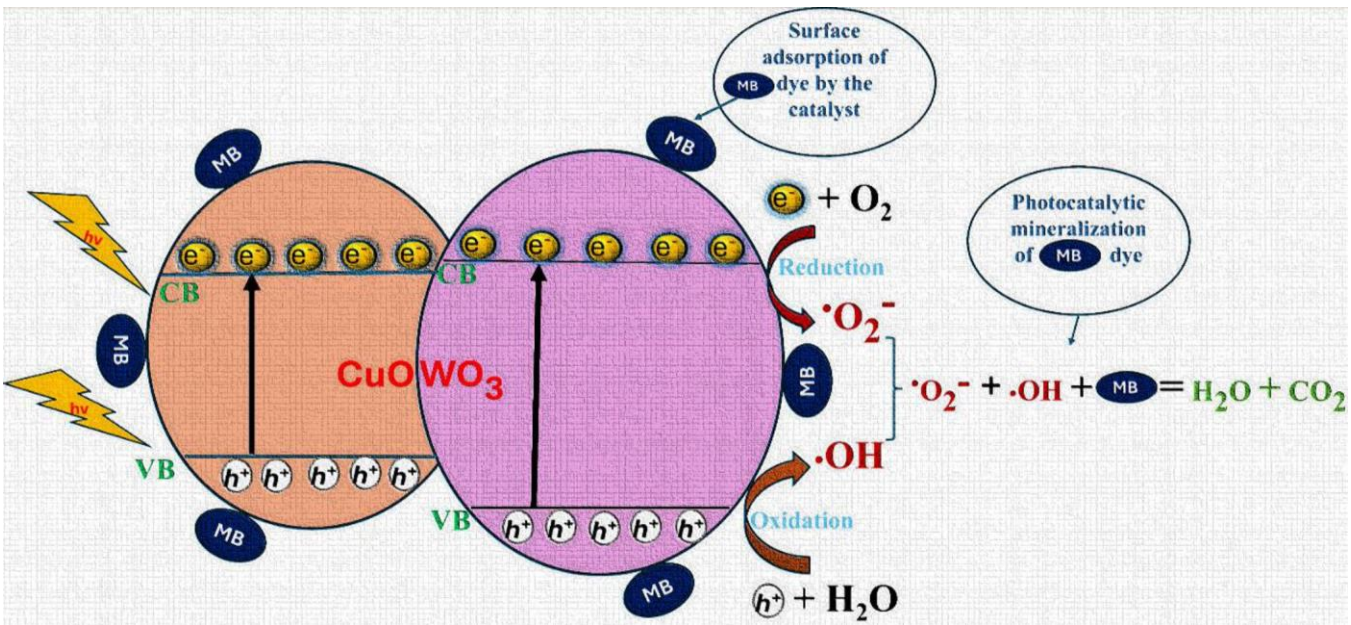

Fig. 11. Photocatalytic degradation mechanism of MB dye using CuO-WO_3 nanocomposite as photocatalyst

TABLE-1
ZONE OF INHIBITION OF SAMPLES AGAINST GRAM-POSITIVE AND NEGATIVE BACTERIA

Sample	*Bacillus*	*Escherichia coli*
Pure CuO	23 mm	15 mm
CuO–WO_3	27 mm	18 mm

oxygen species (ROS) such as hydroxyl radicals and superoxide ions. These ROS induce oxidative stress, disrupt bacterial cell membranes and damage intracellular components, ultimately leading to the bacterial cell death [12].

Furthermore, the heterogeneous morphology and increased surface roughness of the CuO–WO_3 composite enhance physical interaction with bacterial cell walls, improving membrane permeability and accelerating the bacterial inactivation. Consequently, the CuO–WO_3 nanocomposite demonstrates superior antibacterial performance compared to pure CuO. Similar enhancements in antibacterial activity for CuO-WO_3 based nanocomposite under both dark and light conditions have been reported previously [12,15].

Conclusion

Pure CuO and CuO-WO_3 heterostructure nanocomposite have been produced using a simple hydrothermal method. The superior photocatalytic activity of the CuO–WO_3 nanocomposite compared to pure CuO is attributed to the formation of an efficient p–n heterojunction, which enhances charge carrier separation, suppresses electron–hole recombination and promotes higher generation of reactive oxygen species. In addition, improved surface morphology and strong interfacial interaction between CuO and WO_3 further contribute to enhanced dye degradation efficiency and improved catalytic stability. The CuO–WO_3 nanocomposite also exhibits strong antibacterial activity against both Gram-positive and Gram-negative bacteria. These findings demonstrate that heterojunction CuO–WO_3 nanocomposite therefore shows significant potential as a cost-effective and environmentally sustainable material for integrated applications such as wastewater treatment and microbial control in advanced environmental remediation technologies.

CONFLICT OF INTEREST

The authors declare that there is no conflict of interests regarding the publication of this article.

DECLARATION OF AI-ASSISTED TECHNOLOGIES

During the preparation of this manuscript, the authors used an AI-assisted tool(s) to improve the language. The authors reviewed and edited the content and take full responsibility for the published work.

REFERENCES

1. P. Oladoye, T. Ajiboye, E. Omotola and O. Oyewola, *Results Eng.*, **16**, 100678 (2022); https://doi.org/10.1016/j.rineng.2022.100678.
2. K. Dulta, G.K. Ağçeli, P. Chauhan, R. Jasrotia, P.K. Chauhan and J.O. Ighalo, *Sustain. Environ. Res.*, **32**, 2 (2022); https://doi.org/10.1186/s42834-021-00111-w
3. M. Vaseem, A. Umar, Y.B. Hahn, D.H. Kim, K.S. Lee, J.S. Jang and J.S. Lee, *Catal. Commun.*, **10**, 11 (2008); https://doi.org/10.1016/j.catcom.2008.07.022
4. M. Ramesh, *Water Pract. Technol.*, **16**, 1078 (2021); https://doi.org/10.2166/wpt.2021.067.
5. O. Akhavan, *J. Colloid Interface Sci.*, **336**, 117 (2009); https://doi.org/10.1016/j.jcis.2009.03.018
6. S. Subhash and S. Kooriyattil, *J. Mater. Sci. Mater. Electron.*, **36**, 1988 (2025); https://doi.org/10.1007/s10854-025-16053-7
7. D.-H. Gao, Q.-C. Yu, M. Kebeded, Y.-Y. Zhuang, S. Huang, M.-Z. Jiao and X.-J. He, *Rare Met.*, **44**, 1443 (2025); https://doi.org/10.1007/s12598-024-03027-7
8. M.D. Khosravi, M. Ghahari, M. Shafiee Afarani and A.M. Arabi, *Adv. Ceram. Progr.*, **8**, 1 (2022); https://doi.org/10.30501/acp.2022.329820.1082
9. A. Melese, W. Wubet, A. Abebe and A. Hussen, *Results Chem.*, **14**, 102141 (2025); https://doi.org/10.1016/j.rechem.2025.102141
10. M.M. Khin, A.S. Nair, V.J. Babu, R. Murugan and S. Ramakrishna, *Energy Environ. Sci.*, **5**, 8075 (2012); https://doi.org/10.1039/C2EE21818F
11. V.R. Santoyo, P. Serrano-Diaz, B.A. Andrade-Espinoza, Y. Fernández-Arteaga and M.C. Arenas-Arrocena, *Period. Polytech. Chem. Eng.*, **68**, 311 (2024); https://doi.org/10.3311/PPch.36670
12. S. Das and T. Alford, *J. Appl. Phys.*, **113**, 244905 (2013); https://doi.org/10.1063/1.4812584
13. N.R. Dhineshbabu, V. Rajendran, N. Nithyavathy and R. Vetumperumal, *Appl. Nanosci.*, **6**, 933 (2016); https://doi.org/10.1007/s13204-015-0499-2
14. M.A. Abd, R.M.S. Al-Haddad and K.H. Razeg, *J. Univ. Babylon Pure Appl. Sci.*, **27**, 266 (2018).
15. F. Anjum, M. Shaban, M. Ismail, S. Gul, E. Bakhsh, M. Khan, U. Sharafat, S. Khan and M. Khan, *ACS Omega*, **8**, 17667 (2023); https://doi.org/10.1021/acsomega.3c00129
16. H. Yang, *Mater. Res. Bull.*, **142**, 111406 (2021); https://doi.org/10.1016/j.materresbull.2021.111406
17. G. Hosseinzadeh, *J. Water Environ. Nanotechnol.*, **7**, 230 (2022); https://doi.org/10.22090/jwent.2022.03.001
18. V. Dutta, S. Sharma, P. Raizada, V. Thakur, A.A. Khan, V. Saini, A.M. Asiri and P. Singh, *J. Environ. Chem. Eng.*, **9**, 105018 (2021); https://doi.org/10.1016/j.jece.2020.105018
19. S. Dursun, S.N. Koyuncu, İ.C. Kaya, G.G. Kaya, V. Kalem and H. Akyildiz, *J. Water Process Eng.*, **36**, 101390 (2020); https://doi.org/10.1016/j.jwpe.2020.101390
20. S.M. Altanany, M.A. Gondal and U. Baig, *AIP Conf. Proc.*, **1976**, 020014 (2018); https://doi.org/10.1063/1.5042381
21. R. Hosseinzadeh, M. Mohadjerani and S. Mesgar, *IET Nanobiotechnol.*, **11**, 725 (2017); https://doi.org/10.1049/iet-nbt.2016.0241
22. A. Azam, O.M.M. Ahmed, H.S. Khan and A. Memic, *Int. J. Nanomedicine*, **7**, 6003 (2012); https://doi.org/10.2147/IJN.S35347
23. H.C. Ananda Murthy, T.D. Zeleke, K.B. Tan, S. Ghotekar, M.W. Alam, R. Balachandran, K.Y. Chan, P.F. Sanaulla, M.R. Anil Kumar and C.R. Ravikumar, *Results Chem.*, **3**, 100141 (2021); https://doi.org/10.1016/j.rechem.2021.100141
24. A. Ethiraj and D.J. Kang, *Nanoscale Res. Lett.*, **7**, 70 (2012); https://doi.org/10.1186/1556-276X-7-70
25. H. Rehmaan, J. Singh, P. Devi, N. Kishor, N. Kumar, P. Sharma and Anjali, *Asian J. Chem.*, **38**, 45 (2025); https://doi.org/10.14233/ajchem.2026.34785
26. R. Balzer, V. Drago, W.H. Schreiner and L.F.D. Probst, *J. Braz. Chem. Soc.*, **25**, 2026 (2014); https://doi.org/10.5935/0103-5053.20140187
27. H. Zhou, H. Wang, C. Yue, L. He, H. Li, H. Zhang, S. Yang and T. Ma, *Appl. Catal. B*, **344**, 123605 (2024); https://doi.org/10.1016/j.apcatb.2023.123605
28. M. Černík and V.V. Thekkae Padil, *Int. J. Nanomedicine*, **8**, 889 (2013); https://doi.org/10.2147/IJN.S40599

29. S. Sundar, G. Venkatachalam and S.J. Kwon, *Nanomaterials*, **8**, 823 (2018); https://doi.org/10.3390/nano8100823
30. V.B. Kumar and D. Mohanta, *Bull. Mater. Sci.*, **34**, (2011); https://doi.org/10.1007/s12034-011-0117-1
31. K. Syrek, E. Wierzbicka, M. Zych, D. Piecha, M. Szczerba, M. Sołtys-Mróz, J. Kapusta-Kołodziej and G.D. Sulka, *J. Photochem. Photobiol. C: Photochem. Rev.*, **62**, 100681 (2025); https://doi.org/10.1016/j.jphotochemrev.2024.100681
32. H. Fang, Y. Guo, T. Wu and Y. Liu, *New J. Chem.*, **42**, 12779 (2018); https://doi.org/10.1039/C8NJ02052C
33. E. Arulkumar, S. Thanikaikarasan and E.V. Siddhardhan, *Results Chem.*, **7**, 101439 (2024); https://doi.org/10.1016/j.rechem.2024.101439
34. N.D. Dien, P.T. Thu Ha, X.H. Vu, T.T. Trang, T.D. Thanh Giang and N.T. Dung, *RSC Advances*, **13**, 24505 (2023); https://doi.org/10.1039/D3RA03791F
35. P.A. Luque-Morales, A. Lopez-Peraza, O.J. Nava-Olivas, G. Amaya-Parra, Y.A. Baez-Lopez, V.M. Orozco-Carmona, H.E. Garrafa-Galvez and M.J. Chinchillas-Chinchillas, *Materials*, **14**, 7537 (2021); https://doi.org/10.3390/ma14247537
36. P. Raizada, A. Sudhaik, S. Patial, V. Hasija, A.A. Parwaz Khan, P. Singh, S. Gautam, M. Kaur and V.-H. Nguyen, *Arab. J. Chem.*, **13**, 8424 (2020); https://doi.org/10.1016/j.arabjc.2020.06.031
37. H. Berede, D. Andoshe, N. Gultom, D.-H. Kuo, X. Chen, H. Abdullah, T. Wondimu, Y. Wu and O.A. Zelekew, *Sci. Rep.*, **14**, 2314 (2024); https://doi.org/10.1038/s41598-024-52547-w